Biomaterials 257 (2020) 120224

Contents lists available at ScienceDirect

Biomaterials

journal homepage: www.elsevier.com/locate/biomaterials

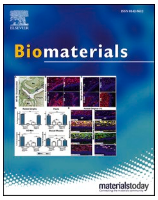

An exosome-like programmable-bioactivating paclitaxel prodrug nanoplatform for enhanced breast cancer metastasis inhibition

Kaiyuan Wang[a,1], Hao Ye[a,1], Xuanbo Zhang[a], Xia Wang[b], Bin Yang[c], Cong Luo[a], Zhiqiang Zhao[a], Jian Zhao[b], Qi Lu[a], Haotian Zhang[d], Qiming Kan[d], Yongjun Wang[a], Zhonggui He[a], Jin Sun[a,*]

[a] *Department of Pharmaceutics, Wuya College of Innovation, Shenyang Pharmaceutical University, Shenyang, Liaoning 110016, PR China*
[b] *School of Pharmacy, Shenyang Pharmaceutical University, Shenyang, Liaoning 110016, PR China*
[c] *State Key Laboratory of Drug Research & Center of Pharmaceutics, Shanghai Institute of Materia Medica, Chinese Academy of Sciences, Shanghai 201203, PR China*
[d] *School of Life Science and Biopharmaceutics, Shenyang Pharmaceutical University, Shenyang, Liaoning 110016, PR China*

ARTICLE INFO

Keywords:
Exosome membrane
Cucurbitacin B
Paclitaxel
Breast cancer metastasis
Programmable bioactivation

ABSTRACT

Metastasis is closely associated with high breast cancer mortality. Although nanotechnology-based anti-metastatic treatments have developed rapidly, the anti-metastasis efficiency is still far from satisfactory, mainly due to the poor recognition of circulating tumor cells (CTCs) in blood. Herein, we developed an exosome-like sequential-bioactivating prodrug nanoplatform (EMPCs) to overcome the obstacle. Specifically, the reactive oxygen species (ROS)-responsive thioether-linked paclitaxel-linoleic acid conjugates (PTX-S-LA) and cucurbitacin B (CuB) are co-encapsulated into polymeric micelles, and the nanoparticles are further decorated with exosome membrane (EM). The resulting EMPCs could specifically capture and neutralize CTCs during blood circulation through the high-affinity interaction between cancer cell membrane and homotypic EM. Following cellular uptake, EMPCs first release CuB, remarkably blocking tumor metastasis via downregulation of the FAK/MMP signaling pathway. Moreover, CuB obviously elevates the intracellular oxidative level to induce a sequential bioactivation of ROS-responsive PTX-S-LA. *In vitro* and *in vivo* results demonstrate that EMPCs not only exhibit amplified prodrug bioactivation, prolonged blood circulation, selective targeting of homotypic tumor cells, and enhanced tumor penetration, but also suppress tumor metastasis through CTCs clearance and FAK/MMP signaling pathway regulation. This study proposes an integrated approach for mechanism-based inhibition of tumor metastasis and manifests a promising potential of programmable-bioactivating prodrug nanoplatform for cancer metastasis inhibition.

1. Introduction

Metastasis is an overwhelming challenge for tumor treatment, accounting for 90% of tumor-caused deaths [1]. Although chemotherapy is a criterion of cancer therapy, small-molecule chemotherapeutic agents exhibit a marginal effect on metastasis inhibition due to the negligible efficiency in eliminating circulating tumor cells (CTCs) [2,3]. CTCs have been proven to aggregate in blood flow to prolong the survival time and construct metastatic lesions [4,5]. The homologous aggregation is mediated by high-affinity interaction between binding proteins overexpressed on the membrane of CTCs [6,7].

Exosomes are 40–180 nm sized extracellular vesicles (EVs) extensively secreted by different kinds of cells, including cancer cells, immune cells, stem cells, and endothelial cells. They play a critical role in long- and short-distance cell-cell communication [8,9]. Various specific surface adhesion molecules are found in the membrane of cancer-derived exosomes, such as CD44, which mediates the homotypic targeting [10] and integrin-associated protein CD47 to escape from macrophage phagocytosis [11]. To the best of our knowledge, exosome-biomimetic nanoparticles have not been reported to eliminate CTCs and for inhibition of tumor metastasis. The strategy of decoration with exosome membrane (EM) could assist nanoparticles in evading macrophage phagocytosis and recognizing both CTCs and primary tumor.

---

* Corresponding author.
E-mail address: sunjin@syphu.edu.cn (J. Sun).

[1] K.W. and H.Y. contributed equally to this work.

https://doi.org/10.1016/j.biomaterials.2020.120224
Received 23 December 2019; Received in revised form 29 June 2020; Accepted 3 July 2020

Due to the overproduction of reactive oxygen species (ROS) in cancer cells, ROS-responsive prodrug strategies aiming to realize tumor-specific bioactivation have developed rapidly in recent years [12,13]. However, the insufficient intrinsic ROS levels within heterogeneous cancer cells hinder the rapid and effective release of parent drug. Therefore, a variety of ROS amplification strategies, including synergistic chemo-photodynamic therapy, Fenton reaction, and glucose oxidase (GOD) co-delivery, have been applied to bioactivate ROS-responsive prodrug [14–17]. In this study, we hypothesize that the sequential-bioactivating prodrug nanoparticles could facilitate ROS-triggered prodrug activation through cucurbitacin B (CuB)-mediated ROS cascade amplification.

CuB is a kind of tetracyclic triterpenoid molecule, extracted from the plant of the Cucurbitaceae family. CuB greatly inhibits the adhesion, migration, and invasion of breast cancer through downregulation of the FAK/MMP signaling pathway [18,19], which is closely associated with extracellular matrix degradation by matrix metalloproteinases (MMPs) to evade the primary tumor and to form the focal adhesion. In addition, CuB mediates rapid and massive ROS generation in various cancer cell lines, contributing to its anticancer and anti-metastasis activity [20].

To test our hypothesis, ROS-sensitive thioether-linked paclitaxel-linoleic acid prodrug (PTX-S-LA) and CuB were co-encapsulated into polyethylene glycol-block-poly(ε-caprolactone) (PEG-PCL) polymeric micelles, which were further decorated with EM to fabricate an exosome-like sequential-bioactivating prodrug nanoplatform (EMPCs). The EMPCs not only effectively target primary tumor but also specifically capture CTCs leading to remarkable metastasis suppression. Following cellular uptake, the nanoparticles would release CuB firstly, significantly blocking the adhesion, migration, and invasion of cancer cells and inhibiting tumor metastasis via FAK/MMP signaling pathway regulation. Furthermore, the released CuB increases ROS levels in tumor cells, contributing to the effective PTX release from PTX-S-LA (Fig. 1). Integrating homotypic EM-mediated CTCs elimination and sequential prodrug bioactivation into a unique biomimetic nanoplatform opens up the opportunity to breast cancer anti-metastasis treatment.

2. Materials and methods

2.1. Materials

PEG5k-PCL15k was obtained from Jinan Daigang Biomaterial Co., Ltd, China. Cucurbitacin B was provided by Chengdu Biopurify Phytochemicals Ltd, China. Paclitaxel was purchased from Nanjing Jingzhu Reagent Co., Ltd, China. Anti-TSG101 antibody, Anti-CD9 antibody and Anti-CD81 antibody were purchased from Beijing Solarbio Science & Technology Co., Ltd, China. Linoleic acid, glycol, 1-hydroxybenzotriazole monohydrate (HOBt), N-(3-dimethylaminopropyl) - N′-ethylcarbodiimide hydrochloride (EDCI) were bought from Aladdin Industrial Co., Ltd, China. 3-(4,5-Dimethythiazol-2-yl)-2,5-diphenyltetrazolium bromide (MTT), 2,7-dichlorodihydrofluorescein diacetate (DCFH-DA), DiI and DiR were purchased from Dalian Meilun Biotech Co., Ltd, China. Anti-CD44 antibody and Anti-CD47 antibody were bought from Biosynthesis Biotechnology Inc. (Beijing, China). Cell culture dishes and plates were obtained from Wuxi NEST Biotechnology Co., Ltd, China. All solvents and reagents applied in the study were analytical grade. Antibodies of FAK/FAK (pTyr-397) were purchased from ABclonal Biotechnology Co., Ltd, China. Antibodies of MMP-2 and MMP-9 were obtained from Abcam Inc., USA. Exosome concentration kits (for cell culture media) was purchased from Liaoning Rengen Biosciences Co., Ltd, China. Scientz-IID Ultrasonic Homogenizer was

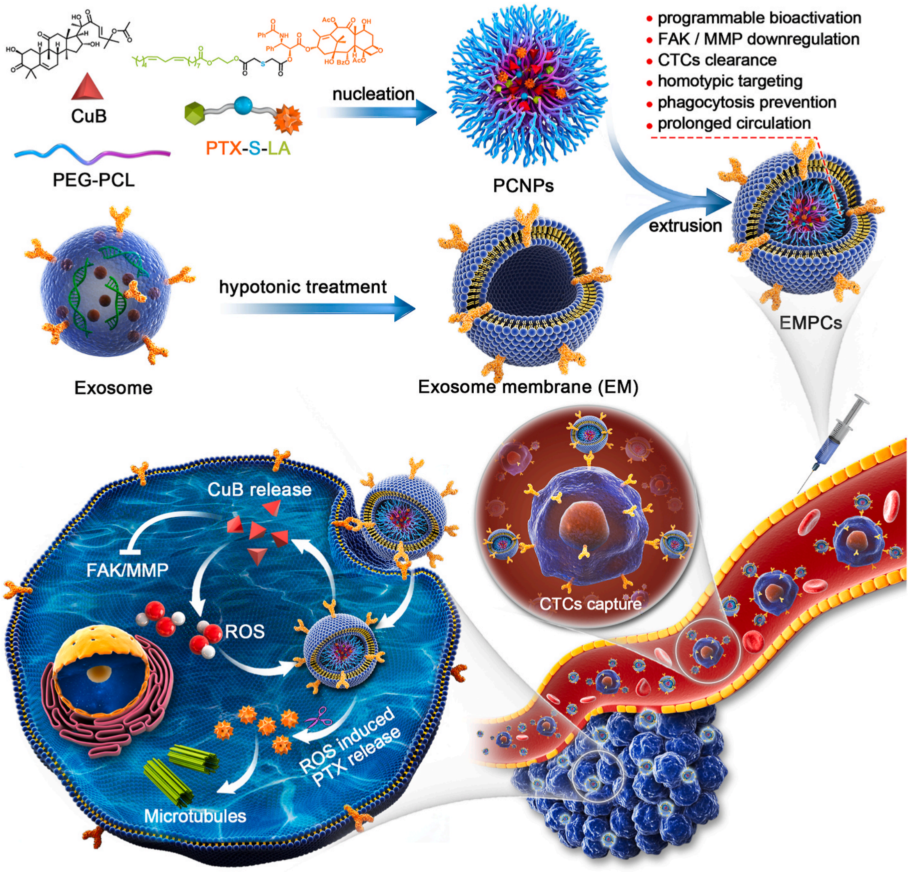

Fig. 1. Schematic representation of the exosome-like sequential-bioactivating paclitaxel prodrug nanoplatform with CTCs clearance, CuB-mediated metastasis suppression, ROS enhancement, and cascade amplified PTX chemotherapy.

purchased from Ningbo Scientz Biotechnology Co., Ltd, China.

2.2. Synthesis of PTX-S-LA

Linoleic acid at a dosage of 2.1 g, 0.43 g of *p*-toluenesulfonic acid, and 38 ml of ethylene glycol were heated to 115 °C under nitrogen for 2 h. The product was extracted using methylbenzene, washed with $NaHCO_3$ solution, and purified by column chromatography. The yield of linoleic acid ethyl ester was 64.9%. Then, 0.22 g of thiodiglycolic anhydride, 0.32 g of EDCI and 0.25 g of HOBt were dissolved with 10 ml of dichloromethane in an ice bath. The linoleic acid ethyl ester was added into the mixture for 35 min of reaction. Next, the temperature was increased to 25 °C and reacted for 12 h. The solution was dried under vacuum. Then, hydrochloric acid was added, and dichloromethane was used to extract product. The dichloromethane layer was washed with NaCl solution. Sodium sulfate was added to dry the product, and the product was purified with column chromatography. The yield of 2′-O-(2-oxo-2-(2-((Z)-linoleoyloxy) ethoxy) ethylsulfenyl) acetic acid was 54.7%. Then, 1.4 g of 2′-O-(2-oxo-2-(2-((Z)-linoleoyloxy) ethoxy) ethylsulfenyl) acetic acid, 0.5 g of EDCI, 0.35 g of HOBt, and 2.2 g of PTX were dissolved into dichloromethane in an ice bath for 3 h and transferred to 25 °C for another 48-h reaction. Eventually, the PTX-S-LA was gained through preparative liquid chromatography, and the yield was 46.1%.

2.3. Preparation of PCNPs and EMPCs

Encapsulation of PTX-S-LA and CuB in PEG-PCL NPs (PCNPs) was conducted by emulsion solvent evaporation approach, where P denotes PTX-S-LA and C denotes CuB. Briefly, 80 mg of PEG-PCL, 4 mg of PTX-S-LA and 0.6 mg of CuB were solubilized in 0.5 ml of acetone. The solution was dropped into 2 ml deionized water with stirring. Acetone was then evaporated under vacuum and large particles were removed using a 220 nm aperture filter. To collect the tumor-derived exosomes, MDA-MB-231 cells were cultured in 37 °C for 2 or 3 days until they grew to 80% confluence. Next, the culture medium was replaced with serum-free medium for 2 days. Then, the medium was collected and centrifuged at 300 g for 10 min to discard cells and further centrifuged at 15,000 g for 30 min to remove cell debris. Following ultracentrifugation at 100,000 g for 120 min, the exosome pellets were acquired. Subsequently, exosomes were resuspended in hypotonic buffer containing protease inhibitor cocktail and stored at 4 °C for 12 h. The mixture was ultracentrifuged at 100,000 g for 5 h to obtain EM. To prepare exosome-biomimetic EMPCs, the mixture of PCNPs and EM was repeatedly co-extruded by a 220 nm polycarbonate porous membrane on an extruder (Antos Nanotechnology Co., Ltd.). The same treatments were applied to fabricate EMPs or EMCs, loaded with PTX-S-LA or CuB, respectively.

2.4. Characterization of PCNPs and EMPCs

The size distribution, polydispersity index, and zeta potential of formulations were detected by dynamic light scattering (DLS, Malvern, U.K.). The morphology of exosomes and different nanoparticles were measured by transmission electron microscope (JEM-2100, JEOL Ltd., Japan). The concentration of PTX-S-LA and CuB loaded in nanoparticles was monitored with high performance liquid chromatography (HPLC). The colloidal stability of EMPCs was investigated in PBS and cell culture media with or without 10% FBS for 24 h at 37 °C. The particle size was detected by DLS at certain intervals. Western blotting for protein moiety identification of EM, EMPs, EMCs, and EMPCs was performed as previously reported. In brief, various molecule weights of proteins were separated with SDS-PAGE electrophoresis. Next, the Coomassie brilliant blue method was applied for gel imaging analysis. In western blotting assay, the proteins were transferred to PVDF membranes; then, the membrane was blocked, and primary antibodies of anti-CD44 and anti-CD47 were added. Following secondary antibodies incubation, ECL Western Blotting Substrate was added for CCD imaging. TSG101, CD9, and CD81 were regarded as markers of exosomes and were also detected with western blotting assay to confirm the success of exosome isolation. The co-localization of the hydrophobic core and EM was applied to investigate the integrity of EM-coated nanoparticles. Coumarin-6 (C-6) was encapsulated in the core of nanoparticles, and DiI was used to stain the EM. The dual-labeled nanoparticles were incubated with MDA-MB-231 cells for 2 h, and the nucleus was stained with Hoechst 33342. Cells were washed using PBS and fixed using 4% paraformaldehyde before confocal laser scanning microscopy (CLSM, C2SI, Nikon, Japan) imaging.

2.5. ROS-responsiveness of PTX-S-LA and in vitro drug release

To test the ROS sensitivity, hydrogen peroxide (H_2O_2) was applied as an ROS simulant. PTX-S-LA dissolved in PBS (pH 7.4) with 30% ethanol, and 0, 2, 5, and 10 mM of H_2O_2 was shaken (120 rpm) at 37 °C. At certain intervals, a 100 μL sample was collected for analysis with HPLC. *In vitro* release study of PTX/CuB from EMPCs was conducted with a dialysis bag (MWCO 14,000) under shaking (120 rpm) at 37 °C and subdivided into four groups: (i) 0 mM of H_2O_2, (ii) 2 mM of H_2O_2, (iii) 5 mM of H_2O_2, and (iv) 10 mM of H_2O_2. Typically, EMPCs were dialyzed against 30 ml of release media. At certain intervals, 100 μL of solution outside the dialysis bag was collected for HPLC analysis. The release study was carried out in triplicate, and results were presented as mean ± SD.

2.6. Cell culture

MDA-MB-231, MCF-7 and RAW264.7 cells were cultured in high-glucose Dulbecco's modified Eagle's medium (DMEM) containing 12% FBS and 1% penicillin/streptomycin (PS). NIH 3T3 cells were cultured in DME/F12 containing 10% FBS and 1% PS. Cells were maintained under conditions of 37 °C and 5% CO_2.

2.7. Cytotoxicity assay

MTT assay was applied to evaluate the antiproliferative activity of Taxol, EMPs, EMCs, and EMPCs against MDA-MB-231 cells. Briefly, cells (1800 cells/well) were seeded in 96-well plates and incubated overnight. Cells were exposed to increasing concentrations of drugs in 200 μL of fresh culture media and incubated for 48 h and 72 h. Then, MTT solution was added to the plate and incubated at 37 °C for 4 h. Finally, the MTT solution was removed, 100 μL of dimethyl sulfoxide (DMSO) was added, and the absorbance was detected with a microplate spectrophotometer at 570 nm.

2.8. Cellular ROS assessment and intracellular drug release

Intracellular ROS production was detected with DCFH-DA staining by inverted fluorescence microscope and flow cytometer. For inverted fluorescence microscope imaging, MDA-MB-231 cells (60,000 cells/well) were cultivated in 24-well plates for 24 h. EMPs, EMCs, or EMPCs were added to cells for 2 h. Subsequently, cells were stained with DCFH-DA for 0.5 h and washed with PBS 3 times. The DCF fluorescence was detected with inverted fluorescence microscope. To further quantify CuB-induced ROS generation, MDA-MB-231 cells (150,000 cells/well) plated onto 12-well plates were treated with EMPs, EMCs, or EMPCs for 2, 6, or 12 h. Subsequently, cells were stained with DCFH-DA for 0.5 h and washed 3 times with PBS. Finally, cells were gathered and resuspended in PBS to monitor the fluorescence signal with a FACS Calibur flow cytometer. To compare the free PTX released from EMPs and EMPCs (PTX equivalent concentration: 500 ng/ml) after incubation with MDA-MB-231 cells for 6 and 24 h, cells together with drug-containing culture media were gathered, and the cells were broken with sonication. After centrifugation, the concentrations of PTX in samples were detected with an ultra performance liquid chromatography-tandem mass spectrometer (UPLC-MS-MS, Waters Co., Ltd, USA). Free PTX operated in the same condition was set as control. The ratio of PTX released from prodrug nanoparticles and PTX detected in control group was PTX release rate.

2.9. *In vitro targeting of MDA-MB-231 cells*

Encapsulation of C-6 in PEG-PCL NPs (C-6 NPs) was conducted by emulsion solvent evaporation approach. Briefly, 40 mg of PEG-PCL and 2 mg of C-6 were solubilized in 0.5 ml of acetone. The solution was dropped into 2 ml deionized water with stirring. Acetone was then evaporated under vacuum. To collect the red blood cells, whole blood withdrawn from the mice was centrifuged at 800 g for 5 min to remove plasma and buffy coat. The resulting red blood cells were washed 3 times in ice cold 1 × PBS and suspended in hypotonic medium of 0.25 × PBS in an ice bath for 30 min. The released hemoglobin was discarded by centrifuging the solution at 12,000 rpm for 5 min. Red blood cell membrane (RM) were collected after washing 3 times by 1 × PBS. To prepare C-6 labeled red blood cell membrane coated PEG-PCL nanoparticles (RM@C-6 NPs) or C-6 labeled EM-coated nanoparticles (EM@C-6 NPs), the mixture of C-6 NPs, RM or C-6 NPs, EM was repeatedly co-extruded by a 220 nm polycarbonate porous membrane on an extruder (Antos Nanotechnology Co., Ltd.).

MDA-MB-231, MCF-7, and NIH 3T3 cells were seeded into 12-well plates. After 24 h of incubation, C-6 NPs, RM@C-6 NPs, or EM@C-6 NPs were added to the wells and incubated for 2 h. Hoechst 33342 was added to stain the nucleus. Subsequently, cells were washed using PBS and fixed using 4% paraformaldehyde before CLSM imaging. To further quantify the homotypic cancer cell targeting efficiency of EM-coated nanoparticles, MDA-MB-231, MCF-7, and NIH 3T3 cells seeded into 12-well plates were exposed to C-6 NPs, RM@C-6 NPs or EM@C-6 NPs for 2 h. Finally, cells were gathered and resuspended in PBS to monitor the fluorescence signal using a FACS Calibur flow cytometer.

2.10. *Cellular uptake of macrophage RAW264.7 cells*

The macrophage RAW264.7 cells were utilized to assess the macrophage phagocytosis evasion ability of nanoparticles. The cells were treated with C-6 NPs, RM@C-6 NPs, and EM@C-6 NPs for 2 h. Before CLSM imaging, cells were washed using PBS and fixed using 4% paraformaldehyde. The quantification of intracellular fluorescence was conducted using a FACS Calibur flow cytometer.

2.11. *Tumor spheroid penetration and wound-healing assay*

The comparison of penetration ability for PEG-PCL nanoparticles and EM-coated nanoparticles was evaluated in three-dimensional MDA-MB-231 spheroids by CLSM. Briefly, 0.5×10^4/well cells suspended in DMEM with 2.5% Matrigel were seeded into ultra-low-attachment 96-well round-bottom plates and centrifuged at 1000 rcf for 10 min. The cells were cultivated under 37 °C and 5% CO_2 conditions for 4 days to form compact spheroids. Next, the C-6 solution, C-6 NPs, and EM@C-6 NPs (33 ng/ml for C-6) were added to tumor spheroids transferred in the confocal dishes and incubated at 37 °C for 8 h. The tumor spheroids were rinsed with ice-cold PBS twice before observation with CLSM. The inhibitory effect of the formulations on migration MDA-MB-231 cells was measured by the wound-healing assay. The 10^5/well cells were seeded into 12-well plates and allowed to grow to 90–95% confluency. The confluent monolayer was scraped with a sterile 200 μL pipette tip to form a cell-free zone. Then, cells were incubated with EMPs, EMCs, and EMPCs (30 nM CuB and 120 nM PTX-S-LA) for the wound-healing assay.

2.12. *Western blotting*

The MDA-MB-231 cells cultured in 6-well plates were incubated with EMPs, EMCs, EMPCs, and blank culture medium as control for 24 h. Radio Immunoprecipitation Assay (RIPA)-lysis buffer was used to acquire cell lysates. The proteins were fractionated with SDS-PAGE electrophoresis, transferred to PVDF and incubated with primary antibodies: *p*-FAK, FAK, MMP-9, MMP-2, and GAPDH at 4 °C overnight. Following secondary antibody incubation, ECL Western Blotting Substrate was added to visualize the protein bands.

2.13. *In vitro capture of CTCs in PBS*

The magnetic beads (MB, MACS, 50 nm) were mixed with EM in PBS. The mixture was repeatedly extruded by a 220 nm polycarbonate porous membrane on an extruder (Antos Nanotechnology Co., Ltd.) to prepare EM-coated magnetic beads (EM@MBs). MDA-MB-231 cells (ie., about 50, 100, 200, 300, and 400 cells) were suspended in 1 ml of PBS and incubated with EM@MBs or MBs for 1 h at 37 °C under 30 rpm. Then, cells were separated by an external magnet and cell numbers were determined by cell count plate (Watson, 177-112C). The cell capture efficiency was defined as the ratio of the captured cells against the total cells.

2.14. *Animal studies*

All experiments were performed in accordance with the guide approved by the Institutional Animal Ethical Care Committee (IAEC) of Shenyang Pharmaceutical University.

2.15. *Pharmacokinetics*

The pharmacokinetic study was conducted with Sprague-Dawley rats (220–270 g, n = 3), which were intravenously administrated with Taxol, PCNPs, EMPCs (4 mg kg^{-1} for PTX) or CuB solution, PCNPs, EMPCs (2 mg kg^{-1} for CuB). Blood samples were collected at timed intervals and centrifuged to get plasma. The concentration of PTX-S-LA, PTX and CuB was monitored with UPLC-MS-MS (Waters Co., Ltd, USA) after protein precipitation.

2.16. *In vivo clearance of CTCs*

Female nude mice were intravenously administrated with saline, PCNPs, and EMPCs (equivalent to 6 mg kg^{-1} PTX and 0.98 mg kg^{-1} CuB). A half hour later, 4×10^5 MDA-MB-231 cells were intravenously injected into the tail vein. At 15 days post-administration, the CTCs in blood were separated through ISET technology with a polycarbonate membrane (Cyclotron, 8 μm) filtration. The number of CTCs was determined by cell count plate (Watson, 177-112C). The elimination efficiency was calculated as the ratio of reducing CTCs number in PCNPs or EMPCs group against remaining CTCs number in saline group. In addition, lungs were excised and stained in Bouin's solution, the visible metastatic nodules was quantified. Hematoxylin and eosin (H&E) staining was also applied to detect the lung metastasis.

2.17. *Study of MDA-MB-231 xenograft tumor model*

To establish the MDA-MB-231 back tumor model, MDA-MB-231 cells (1×10^7 cells) were subcutaneously implanted into the right back side of female nude mice. For the biodistribution experiment, the mice bearing tumor cells were divided into two groups. When the tumor volume reached approximately 300 mm^3, the DiR-labeled PEG-PCL nanoparticles (DiR NPs) and DiR-labeled EM-coated nanoparticles (EM@DiR NPs) at 2 mg DiR/kg were injected intravenously. Fluorescence imaging was performed at different time intervals (2 h, 8 h, 12 h, 24 h) post intravenous injection using *in vivo* imaging system (IVIS). At 24 h post injection, the mice were sacrificed, and the fluorescence imaging in the major organs (heart, liver, spleens, lungs, kidneys) and tumors were analyzed by IVIS. For *in vivo* antitumor study, the animals ($n = 5$) received tail vein injections of the various drug formulations (saline, Taxol, EMCs, EMPs, PCNPs, and EMPCs, equivalent to 6 mg kg^{-1} PTX and 0.98 mg kg^{-1} CuB) every 3 days for 30 days once the tumor size reached an average volume of 100 mm^3. During the treatment, the tumor size was calculated using formula $V = 1/2\ ab^2$ (a: long axis, b: short axis), and body weight was monitored. Mice were sacrificed after 30 treatment days, and their lungs were collected and stained in Bouin's solution. The heart, liver, spleen, lungs, kidneys and tumor of one mouse in every group was excised and sliced for H&E staining. The weight of the tumor was recorded.

2.18. *Study of MDA-MB-231 orthotopic tumor model*

To establish the MDA-MB-231 orthotopic tumor model, 1×10^7 MDA-MB-231-luc cells were injected into the mammary fat pads of female nude mice. The orthotopic biodistribution study and orthotopic *in vivo* antitumor experimental profiles were similar to that of the subcutaneous breast cancer xenografts. After 30 treatment days in the orthotopic antitumor experiment, mice were sacrificed, and fresh lungs were collected and incubated in 15 mg ml^{-1} D-luciferin for 10 min to assess the anti-metastasis effect. The *ex vivo* bioluminescent imaging of lungs was performed with IVIS. To further detect the prodrug bioactivation in tumor tissue, MDA-MB-231 orthotopic tumor-bearing mice were divided into two groups. EMPs and EMPCs (equivalent to 6 mg kg^{-1} PTX and 0.98 mg kg^{-1} CuB) were administered intravenously once

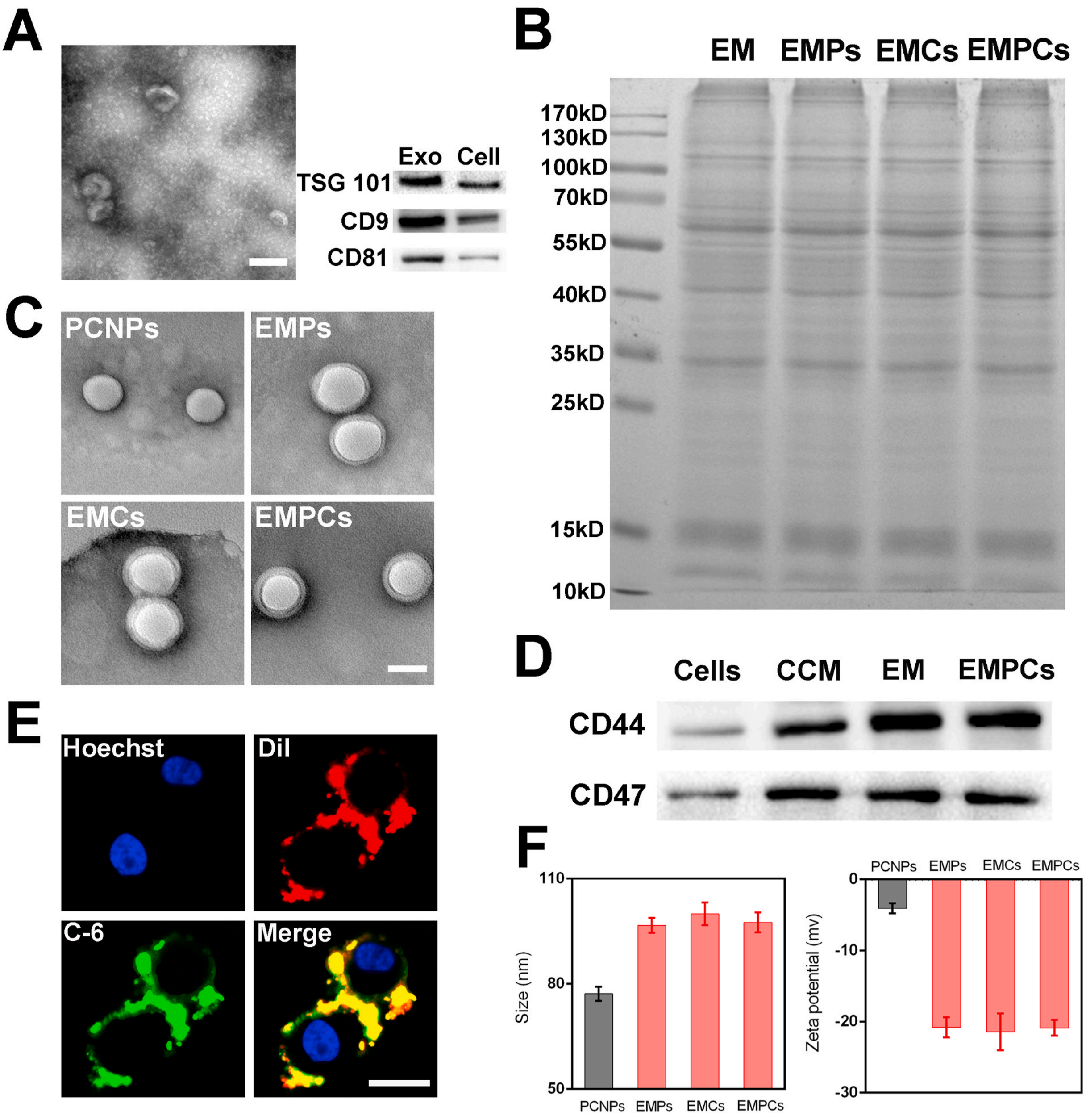

Fig. 2. (A) TEM image and detection of TSG101, CD9, and CD81 proteins for MDA-MB-231 derived exosomes. Scale bar = 100 nm. (B) SDS-PAGE protein analysis of EM, EMPs, EMCs and EMPCs. (C) TEM images of PCNPs, EMPs, EMCs, and EMPCs. Scale bar = 100 nm. (D) Western blotting analysis of whole MDA-MB-231 cells, MDA-MB-231 cancer cell membrane (CCM), EM and EMPCs, for CD44 and CD47 proteins. (E) Intracellular co-localization of EM shell (red) and PEG-PCL core (green). Scale bar = 10 μm. (F) Hydrodynamic diameter and zeta potential of PCNPs, EMPs, EMCs and EMPCs. (For interpretation of the references to colour in this figure legend, the reader is referred to the Web version of this article.)

the tumor volume reached approximately 300 mm^3. Mice were sacrificed at 12 h post-administration, and tumors were collected. The concentration of released PTX was monitored with UPLC-MS-MS (Waters Co., Ltd., USA) after homogenization and protein precipitation.

3. Results and discussion

3.1. Preparation and characterization of the nanosystem

Firstly, the ROS-sensitive PTX prodrug was prepared by conjugating linoleic acid to PTX by a single thioether linkage (Scheme S1). The chemical structure was verified with MS and ^{1}H NMR (Fig. S1). The PTX-S-LA and CuB were co-loaded into PEG-PCL nanoparticles using the emulsion solvent evaporation approach to fabricate PCNPs [21–23], where P denotes PTX-S-LA and C denotes CuB. The PCNPs were then incubated with EM to acquire the EMPCs. The same treatments were applied to fabricate EMPs or EMCs, loaded with PTX-S-LA or CuB, respectively. Fig. 2 displayed the hydrodynamic diameter and morphology of PCNPs, which had a regular spherical shape with an average size of nearly 80 nm. The drug-loading capacities of PTX-S-LA

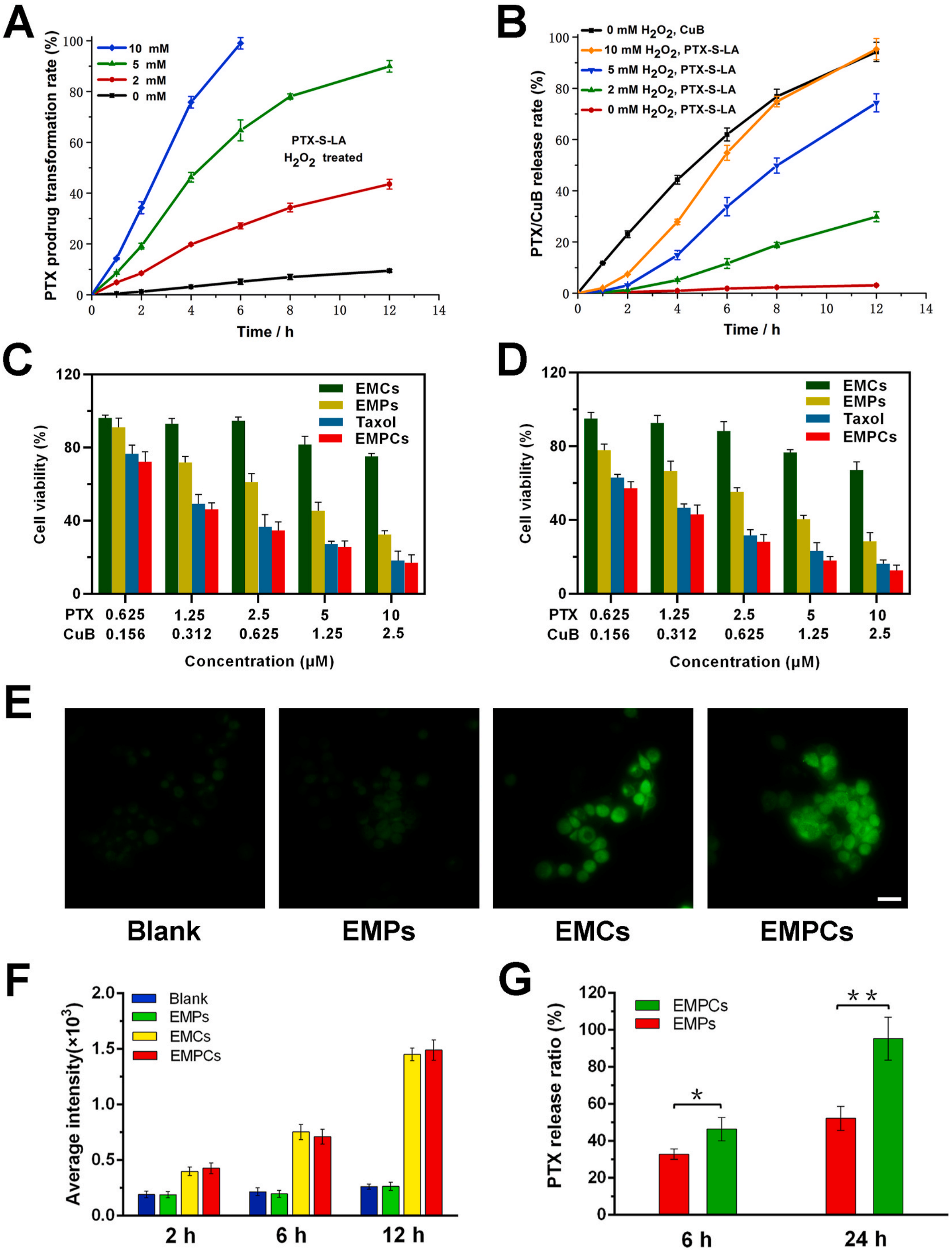

Fig. 3. (A) Transformation of PTX-S-LA into PTX in the presence of H_2O_2. (B) In vitro drug release profiles of CuB and PTX from EMPCs with various concentrations of H_2O_2. Cytotoxicity of EMCs, EMPs, Taxol, and EMPCs against MDA-MB-231 cells for (C) 48 h and (D) 72 h. (E) Fluorescence microscopy images and (F) flow cytometry analysis of MDA-MB-231 cells stained with DCFH-DA after incubation with blank culture medium, EMPs, EMCs, or EMPCs. Scale bar = 20 μm. (G) PTX release amount of EMPs and EMPCs in MDA-MB-231 cells after 6 h and 24 h incubation (**$P < 0.01$, *$P < 0.05$, $n = 3$).

and CuB in PEG-PCL nanoparticles were 9 wt% and 5 wt%, and the encapsulation efficiency were 87.6% and 69.2%, respectively.

The gradient centrifugation method was used to extract exosomes. The saucer-like structure of exosomes by transmission electron microscopy (TEM) imaging together with western blotting analysis for characteristic exosome markers TSG101, CD9, and CD81, indicated the successful isolation of exosomes [24]. EM was prepared via the hypotonic treatment of extracted exosomes. The PEG-PCL nanoparticles were further incubated with EM to prepare EMPCs [25]. The decreased zeta potential, increased particle size (~100 nm), and TEM images demonstrated the decoration of EM on the surface of PEG-PCL nanoparticles. Fig. S2 showed that EMPCs had desirable colloidal stability after incubation in phosphate-buffered saline (PBS) and cell culture media with or without 10% fetal bovine serum (FBS) for 24 h.

To examine the existence of membrane proteins on the shell of exosome-biomimetic nanoparticles, sodium dodecyl sulfate polyacrylamide gel electrophoresis (SDS-PAGE) and western blotting assay were performed as previously reported [26]. SDS-PAGE protein examination of the membrane protein markers showed good preservation of the distinctive proteins inherited from EM in the protein profile of exosome-biomimetic nanoparticles. CD44 and CD47 are of critical importance for tumor metastasis. CD44 is a surface adhesion molecule on MDA-MB-231 cells, which plays a crucial role in the adherence of CTCs to metastasis lesions. CD47 could protect tumor cells from macrophage phagocytosis, which is associated with tumor aggression. As shown in Fig. 2D, they co-existed on the cancer cell membrane and EM and were conserved well in EMPCs to mediate homotypic cancer cell targeting.

Then, EM was labeled with DiI (red), and the hydrophobic core was labeled with coumarin-6 (C-6, green) to examine the complete coating of PEG-PCL nanoparticles with EM [27]. The dual-labeled nanoparticles were added to MDA-MB-231 cells for 2 h and observed with confocal laser scanning microscopy (CLSM). As shown in Fig. 2E, the fluorescence of DiI was co-localized with that of C-6, indicating that exosome-biomimetic nanoparticles could retain the structural integrity after cellular uptake for a period of time.

3.2. *ROS-responsiveness of PTX-S-LA and in vitro drug release*

To investigate the ROS-responsiveness of PTX-S-LA, H_2O_2 was used as an ROS simulant [28]. As shown in Fig. 3A, only 10% PTX was released from PTX-S-LA after 12 h of incubation without H_2O_2. In comparison, PTX-S-LA released nearly 100% of PTX in the presence of 10 mM of H_2O_2 within 6 h, suggesting an excellent ROS-sensitive bioactivation capability of PTX-S-LA. Furthermore, EMPCs were incubated with different concentrations of H_2O_2 to explore the sequential-bioactivation process [29]. Approximately 94% of CuB was released faster than PTX-S-LA (4%) after 12 h of incubation in the absence of H_2O_2. By contrast, after the addition of H_2O_2, the PTX release percentage of PTX-S-LA increased in an H_2O_2 concentration-dependent manner and dramatically reached 95% in 12 h after incubation with 10 mM of H_2O_2 (Fig. 3B).

3.3. *Cytotoxicity assay*

We subsequently detected the cytotoxicity in MDA-MB-231 cells with MTT assay. The Chou-Talalay method is now the most widely used method in the literature for analyzing combinations. The combination index (CI) was calculated according to equation below: $CI = (D)_1/(Dx)_1 + (D)_2/(Dx)_2$, in which the denominator $(Dx)_1$ and $(Dx)_2$ are the concentration of Drug 1 and Drug 2 alone that inhibit the growth of cells by x %. Similarly, the numerator $(D)_1$ and $(D)_2$ represent the respective dosage of Drug 1 and Drug 2 at which their drug combo inhibits the cell growth by the same x %. $CI < 1$, $CI = 1$, and $CI > 1$ represents synergism, additive effect, and antagonism, respectively. The growth inhibition effect (fraction affected, Fa) was calculated according to equation below: Fa = 1-(%growth/100). A plot of CI values at different levels of growth inhibition effect (fraction affected, Fa) can be determined by computer simulation. Such a combination index plot is also called the Fa–CI plot. In Fig. S3, the plots showed that molar ratio 4:1 of PTX-S-LA to CuB has the best synergism at the most effect level (Fa). Fig. 3C and D showed that the cytotoxicity of EMPs was much lower than that of Taxol due to the delayed prodrug bioactivation. This was resulted from the blocking of C2′-hydroxyl, essential to the antitumor efficacy of PTX. By contrast, EMPCs displayed better cancer cell killing capability in comparison with Taxol. As shown in Table S1, the half maximal inhibitory concentration (IC_{50}) at the equivalent concentrations of PTX were 4206 nM and 1365 nM for EMPs and EMPCs, in comparison with 1572 nM for Taxol at 48 h against MDA-MB-231 cells. Moreover, the CI values of EMPCs against MDA-MB-231 cells were 0.37 and 0.31 for 48 h and 72 h, suggesting a strong synergic effect and good sequential prodrug bioactivation.

3.4. *Cellular ROS assessment and intracellular drug release*

To investigate the ROS generation, MDA-MB-231 cells incubated with different formulations were stained by 2,7-dichlorodihydrofluorescein diacetate (DCFH-DA). The ROS level exhibited no enhancement after incubation with EMPs, while CuB-loaded EMCs and EMPCs considerably improved intracellular ROS levels (Fig. 3E). To further quantify the CuB-induced ROS production, the fluorescence intensity was detected with flow cytometry after 2, 6, or 12 h of treatment. The EMCs and EMPCs remarkably improved the intracellular ROS level in a time-dependent manner within 12 h (Fig. 3F). Therefore, the co-loaded CuB could enhance ROS levels in MDA-MB-231 cells, further increasing prodrug bioactivation. Encouraged by the results of ROS detection, we further monitored the released PTX from EMPCs and EMPs after 6 or 24 h incubation with MDA-MB-231 cells. As shown in Fig. 3G, the PTX release amount of EMPCs was much higher than that of EMPs, agreeing well with the *in vitro* drug release result.

3.5. *In vitro targeting of MDA-MB-231 cells*

We next investigated the cellular uptake of C-6 labeled PEG-PCL nanoparticles (C-6 NPs), C-6 labeled red blood cell membrane coated PEG-PCL nanoparticles (RM@C-6 NPs) and C-6 labeled EM-coated nanoparticles (EM@C-6 NPs) in MDA-MB-231, MCF-7, and NIH 3T3 cells to confirm the homotypic cancer cell targeting capability of exosome-biomimetic nanoparticles. The decoration of PEG-PCL nanoparticles with red blood cell membrane was conducted to verify the critical role of proteins on EM in promoting internalization of MDA-MB-231 cells. As shown in Fig. 4A, the C-6 fluorescence of C-6 NPs and RM@C-6 NPs was rather lower than that of EM@C-6 NPs, demonstrating that the improved cellular uptake was attributed to proteins on EM. Meanwhile, MCF-7 and NIH 3T3 cells were set as the negative controls. No formulation exhibited improvement of green fluorescence in MCF-7 and NIH 3T3 cells, further illustrating that the decoration of nanoparticles with EM specifically enhanced internalization of the same-source cancer cells. The quantification of targeting effect was then detected with flow cytometry. As shown in Fig. 4B and Fig. S4, the fluorescence signal of EM@C-6 NPs was 3.5 times higher than those of C-6 NPs and RM@C-6 NPs in MDA-MB-231 cells. By contrast, EM@C-6 NPs showed no increase of fluorescence in MCF-7 and 3T3 cells in comparison with C-6 NPs and RM@C-6 NPs. All results mentioned above indicated that exosome-biomimetic nanoparticles had a selective affinity to the homotypic cancer cells.

3.6. *Cellular uptake of macrophage RAW264.7 cells*

Then, we verified the macrophage phagocytosis evasion ability of CD47 on EM. Mouse macrophage RAW264.7 cells seeded into 12-well plates were incubated with C-6 NPs, RM@C-6 NPs and EM@C-6 NPs.

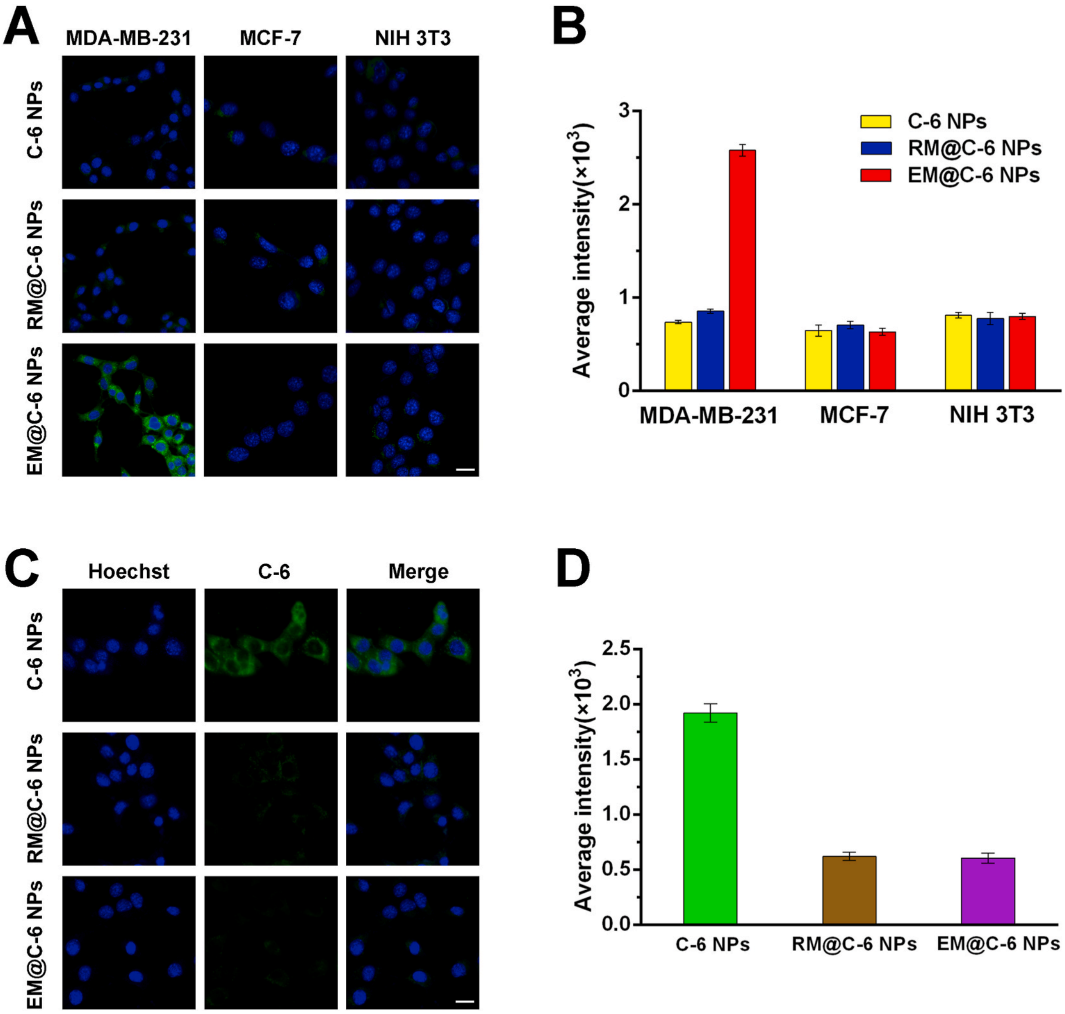

Fig. 4. (A) CLSM images and (B) flow cytometry analysis of MDA-MB-231, MCF-7, NIH 3T3 cells incubated with C-6 NPs, RM@C-6 NPs, and EM@C-6 NPs. The nucleus was stained with Hoechst (blue), and nanoparticles were labeled with C-6 (green). (C) Intracellular uptake imaging and (D) intracellular fluorescence intensity detected with flow cytometry of C-6 NPs, RM@C-6 NPs and EM@C-6 NPs incubated in macrophage RAW264.7 cells for 2 h. Scale bar = 15 μm. (For interpretation of the references to colour in this figure legend, the reader is referred to the Web version of this article.)

As shown in Fig. 4C, the RM@C-6 NPs and EM@C-6 NPs exhibited a much lower internalization than C-6 NPs. For flow cytometry quantification, the fluorescence intensity of C-6 NPs displayed a 3.1-fold increase in comparison with that of RM@C-6 NPs and EM@C-6 NPs. The results confirmed that the CD47 on both RM and EM could inhibit the macrophage phagocytosis.

3.7. *Tumor spheroid penetration and wound-healing assay*

MDA-MB-231 cells spheroids were performed to assess the tumor spatial penetration ability of exosome-biomimetic nanoparticles [30]. The spheroids were incubated with C-6 solution, C-6 NPs, and EM@C-6 NPs for 8 h. CLSM images exhibited that the fluorescence signal of C-6 from EM@C-6 NPs was higher in the deep site of cancer cells spheroids than that of C-6 solution and C-6 NPs (Fig. 5A), demonstrating an in-depth tumor penetration capability of exosome-biomimetic nanoparticles. Since the cancer cell migration was associated with tumor metastasis, the migration inhibition effects of different formulations (control, EMPs, EMCs, and EMPCs) were examined on MDA-MB-231 cells through wound healing trials. After 24 h treatment, the wound gap had nearly disappeared in the control group. Moreover, the cell migration capability was remarkably suppressed in EMCs- and EMPCs-treated groups compared with the EMPs group (Fig. 5B), demonstrating the good anti-metastasis effect of CuB.

3.8. *Western blotting*

Western blotting assay was conducted to monitor the expression levels of key molecules related to tumor metastasis. Previous studies have clarified the role of the FAK/MMP signaling pathway in cancer migration and invasion, including extracellular matrix degradation by matrix metalloproteinases (MMPs) to evade primary tumor and to form the focal adhesion. To evaluate the FAK/MMP signaling pathway suppression caused by different formulations, we detected the expression of activated FAK (phospho-FAK, *p*-FAK), FAK, MMP-9, and MMP-2 in cell lysates. In agreement with the wound healing assay, EMCs and EMPCs significantly suppressed the FAK/MMP signaling pathway compared with EMPs (Fig. 5C), further confirming the CuB-mediated anti-metastasis effect.

3.9. *Pharmacokinetics*

We next investigated the pharmacokinetic profiles of Taxol, CuB solution, PCNPs, and EMPCs in Sprague-Dawley rats. As presented in Fig. 5D, Fig. S5 and Table S2, PTX and CuB were eliminated rapidly from blood circulation after intravenous administration of Taxol or CuB solution. EMPCs and PCNPs showed extended blood circulation time in comparison with Taxol or CuB solution. Surprisingly, EMPCs exhibited an approximately 2-fold increase in the area under the curve (AUC) of

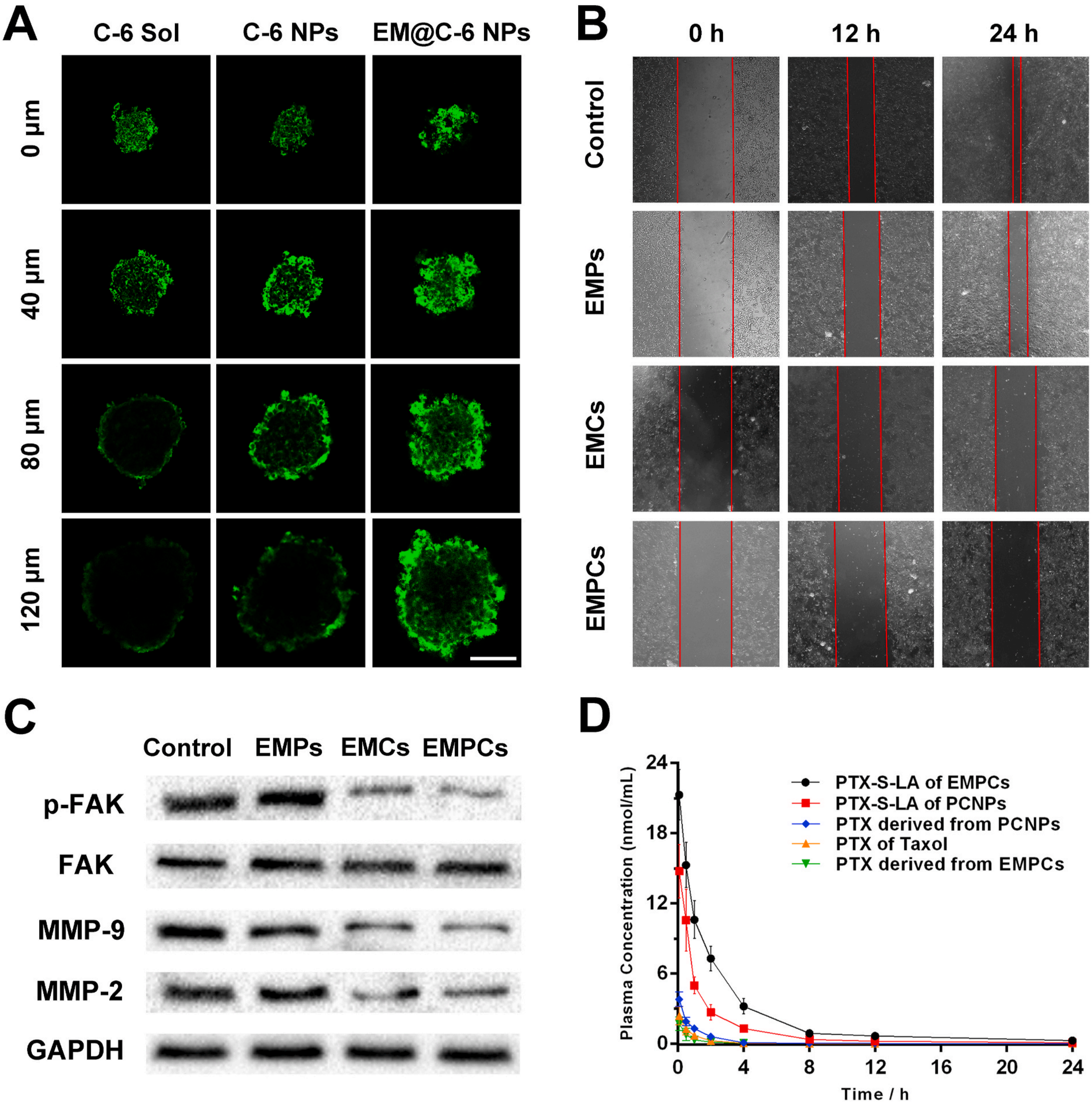

Fig. 5. (A) *In vitro* penetration of C-6 solution, C-6 NPs and EM@C-6 NPs incubated with MDA-MB-231 tumor spheroids. Scale bar = 100 μm. (B) Typical images of wound healing assessments of control, EMPs, EMCs, and EMPCs on MDA-MB-231 cells at 0, 12, and 24 h. (C) The effect of EMPs, EMCs, and EMPCs on the expression levels of FAK/MMP signaling pathway proteins. (D) Drug concentration in plasma as a function of time after a single intravenous injection of Taxol, PCNPs, or EMPCs.

PTX-S-LA and CuB as well as longer half-life compared with PCNPs, suggesting that the self-protection ability of CD47 on EM significantly suppressed macrophage phagocytosis. Moreover, EMPCs decreased the undesired leakage of PTX during blood circulation compared to PCNPs, demonstrating an enhanced systemic safety of EM-coating nanoparticles.

3.10. *In vitro capture of CTCs in PBS*

Then, magnetic beads (MBs) and EM-coated magnetic beads (EM@MBs) were prepared to investigate the *in vitro* CTCs capture ability of EM-biomimetic nanoparticles. After 1 h co-incubation with MDA-MB-231 cells under 30 rpm, an external magnet was used to separate the captured cells. It is worth noting that regression analysis showed a much higher CTCs capture efficiency of EM@MBs (Fig. 6A), which could be attributed to the adhesion molecule CD44 on EM.

3.11. *In vivo clearance of CTCs*

Encouraged by *in vitro* study, we examined the potential of EMPCs to eradicate CTCs in the circulatory system. The experiments were carried out using nude mice with an inhibited immune system. After intravenous administration with saline, PCNPs, and EMPCs, mice were then intravenously injected with MDA-MB-231 cells as CTCs simulant [31]. At 15 days post-administration, the CTCs in blood were separated through ISET technology [32] with a polycarbonate membrane (Cyclotron, 8 μm) filtration. As shown in Fig. 6B, the CTCs elimination efficiency of EMPCs was 3.2 times higher than that of PCNPs, confirming the excellent *in vivo* CTCs clearance ability of EMPCs. CTCs in blood could spread to various major organs, particularly the lungs. As shown in Fig. 6C and D, mice treated with saline had remarkable micro-metastases in the lungs. The lung micro-metastases number of mice treated with PCNPs showed a slight reduction. By contrast, there

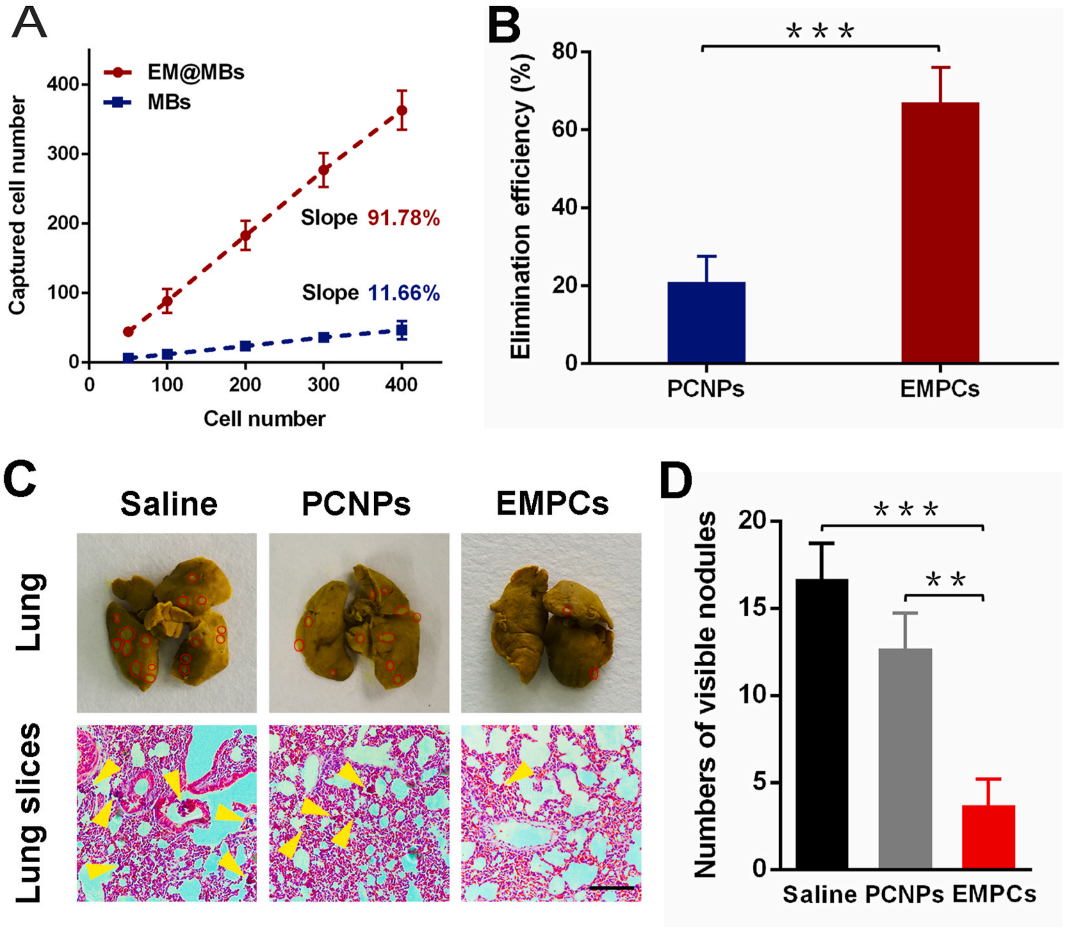

Fig. 6. (A) *In vitro* CTCs capture efficiency of EM@MBs and MBs in PBS. (B) *In vivo* CTCs elimination efficiency of PCNPs and EMPCs (***P < 0.001, n = 5). (C) Photos of Bouin's solution stained whole lungs and H&E staining of the lung slices collected from saline, PCNPs and EMPCs groups. Red circles demonstrate the visible metastatic site. Yellow arrows demonstrate the lung metastases. Scale bar = 100 μm. (D) Quantification of visible metastatic nodules (***P < 0.001, **P $<$ 0.01, n = 5). (For interpretation of the references to colour in this figure legend, the reader is referred to the Web version of this article.)

was negligible metastatic nodule observed in the lung of EMPCs-treated mice, indicating that EMPCs could target the CTCs during systemic circulation through adhesion molecule CD44 and further neutralize the CTCs via sequential prodrug bioactivation.

3.12. Study of MDA-MB-231 xenograft tumor model

To investigate the tumor-targeting capability of exosome-biomimetic nanoparticles, an MDA-MB-231 xenograft tumor model was employed [33]. As shown in Fig. S6, the fluorescence intensity of DiR-labeled EM-coated nanoparticles (EM@DiR NPs) increased over time from 2 h to 12 h, notably stronger than that of DiR-labeled PEG-PCL nanoparticles (DiR NPs). Moreover, the *ex vivo* fluorescence of EM@DiR NPs in tumor tissue remained high at 24 h post administration, a 3.6-fold increase in comparison with that of DiR NPs. The enhanced tumor accumulation of exosome-biomimetic nanoparticles was due to homotypic targeting capability and prolonged blood circulation time.

We further investigated the *in vivo* antitumor efficacy of EMPCs with MDA-MB-231 back tumor-bearing mice. As shown in Fig. S7, the control group exhibited a quick increase in tumor volume (~1400 mm^3 at day 30). Within 30 d, the volume of the tumor increased to ~1000 mm^3 and ~800 mm^3 in EMC and Taxol groups, indicating a moderate tumor-inhibitory ability. The tumor volume reached ~520 mm^3 and ~300 mm^3 for the EMPs and PCNPs groups after 30 d of treatment. In contrast, EMPCs indicated a complete tumor growth inhibition (~130 mm^3 at day 30), exhibited the strongest induction of tumor apoptosis in H&E stained tumor slices (Fig. S8), and highlighted the advantages of CuB-mediated strengthened PTX chemotherapy and EM-related excellent tumor-targeting capability. Bouin's solution staining and H&E staining were applied to compare the potential of different formulations to suppress tumor metastasis *in vivo*. As presented in Fig. S7D, no evident cancer metastasis was observed in the EMPCs group. The Taxol, EMPs, and PCNPs groups showed serious tumor metastases in the lungs and liver, but there was a significant reduction of metastatic nodules in the EMCs group, clarifying the EM-mediated CTCs targeting and CuB-related metastasis inhibition.

3.13. Study of MDA-MB-231 orthotopic tumor model

We then compared the tumor-targeting ability of DiR NPs and EM@DiR NPs in orthotopic MDA-MB-231 tumor-bearing mice. The EM@DiR NPs exhibited the highest fluorescence signal at tumor site after 12 h administration, much stronger than that of DiR NPs. Moreover, the *ex vivo* fluorescence intensity of EM@DiR NPs in tumor tissue showed a 3.1-fold increase compared with that of DiR NPs, implying an excellent targeting ability of exosome-biomimetic nanoparticles. Encouraged by biodistribution results, the bioactivated PTX release performance in tumor tissue was further monitored. As shown in Fig. 7D, the concentration of released PTX in the EMPCs group was 2.9 times higher than that of the EMPs group, further confirming the *in vivo* CuB-mediated amplified prodrug bioactivation.

The therapeutic efficacy was further evaluated in orthotopic MDA-MB-231-luc tumor-bearing mice treated with various formulations. As shown in Fig. 8A, the tumor volume evidently increased to ~1530 mm^3

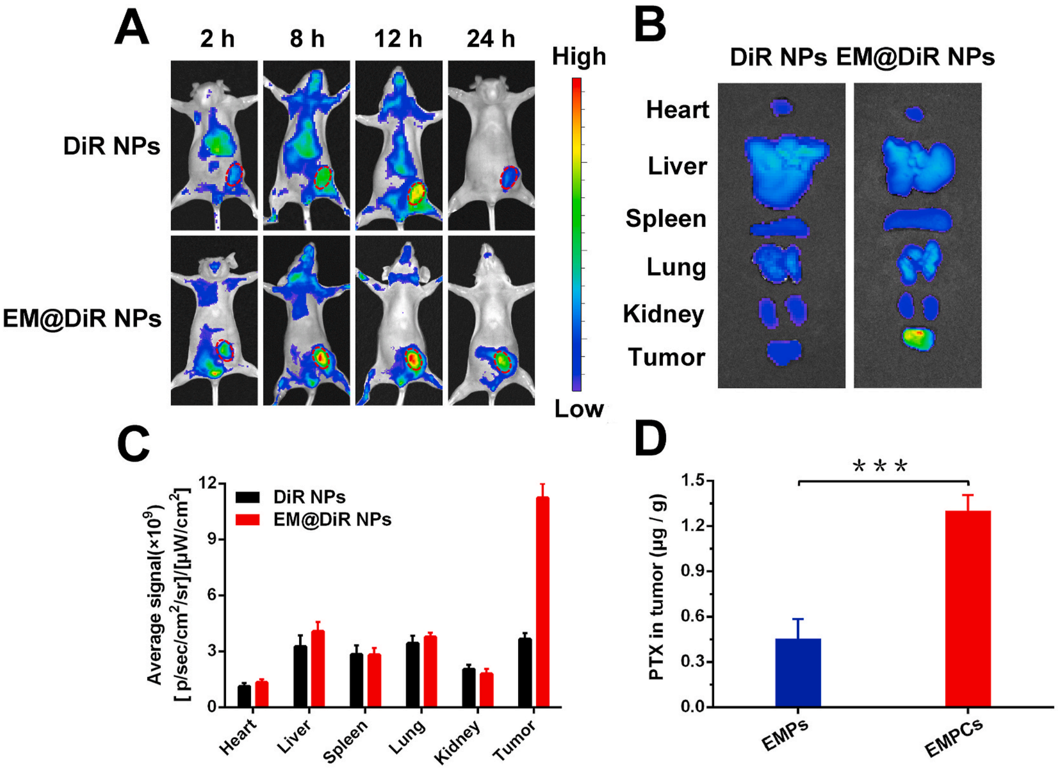

Fig. 7. In vivo fluorescence imaging in orthotopic MDA-MB-231 tumor-bearing mice at 2, 8, 12, and 24 h following injection with DiR NPs and EM@DiR NPs. (B) Ex vivo fluorescence imaging and (C) ROI analysis of major organs and tumors harvested at 24 h post-administration. (D) PTX release amount of EMPs and EMPCs in tumors at 12 h after injection (***P < 0.001, n = 3).

from an initial value of 100 mm^3 in the saline-treated group. The tumor volume of EMCs and Taxol reached ~1150 mm^3 and ~1000 mm^3 within 30 d, suggesting poor tumor suppression. EMPs and PCNPs produced a significant decrease in tumor volume, and the tumor sizes were ~710 mm^3 and ~430 mm^3 at the end of 30 d of treatment. Furthermore, EMPCs displayed the best antitumor activity (~210 mm^3 at day 30) and the severest apoptosis of tumor tissue in H&E stained tumor slices (Fig. S9), proving the important role of EM-related homotypic targeting and CuB-mediated facilitated prodrug bioactivation in tumor growth suppression.

To verify the anti-metastatic activity of EMPCs, the excised lungs were analyzed with IVIS bioluminescence after 30 d of treatment [34]. As shown in Fig. 8D, the saline and Taxol groups exhibited serious lung metastasis and high bioluminescent intensities. By contrast, the bioluminescent signal of the EMPs and PCNPs groups were decreased to a certain extent. Unlike the increase in tumor volume, bioluminescent intensity of EMCs group was similar to that of EMPCs group, indicating the potent CTCs targeting of EM-coating and anti-metastasis of loaded CuB. As shown in Fig. 8E, the Bouin's solution staining and H&E staining results further confirmed the outstanding anti-metastasis ability of EMCs, which displayed less tumor metastases in the lungs and liver than that of the saline, Taxol, EMPs, and PCNPs groups. Moreover, the EMPCs group exhibited no obvious cancer metastasis in lung and liver tissues. Therefore, EM-coating CuB-loaded nanoparticles could serve as a promising nanoplatform for highly efficient breast cancer metastasis inhibition and introduced cascade-amplified bioactivation in prodrug nanoplatform strategy.

The highly homotypic targeting interaction can be achieved between the EMPCs and the source tumor cells, resulting in efficient CTCs capture and enhanced tumor accumulation. With the development of modern medicine, the personalized treatment of cancer has attracted more and more attention from researchers and patients. It is expected to introduce the strategy of EM decoration into personalized treatment. The tumor cells isolated from patient could be cultured *in vitro* to produce efficient patient-derived EMPCs. However, the efficiency of EM extraction may restrict the large-scale clinical application of EMPCs. Meanwhile, the batch-to-batch variation would influence the therapeutic effect. Currently, the capacity of exosomes has spurred a broad interest in their utility as a delivery system for various therapeutics. And some effort has been made to develop high scale and efficient production of personalized exosome preparations. For example, Mendt et al. reported a process for large-scale production of clinical-grade exosomes employing good manufacturing practice (GMP) standards [35]. The clinical-grade GMP exosomes were tested in multiple *in vitro* and *in vivo* studies to confirm the suppression of oncogenic Kras and an increase in the survival of several mouse models with pancreatic cancer. In our follow-up research, we would spend more effort on producing personalized clinical-grade exosome preparation. And we believe that more and more exosome-based antitumor preparations would enter into clinical practice.

4. Conclusions

In summary, we developed an exosome-like programmable-bioactivating prodrug nanoplatform for breast cancer anti-metastatic treatment. It is well known that approximately 90% death of tumor is caused by the secondary tumor. The metastatic process is comprised of the following steps: neoangiogenesis, intravasation, circulation in the peripheral blood, extravasation, and ultimately resulting in colonization and growth at distant sites. Obviously, CTCs act as the "vector" of metastasis, and the successful capture and elimination of the CTCs is of great importance. The biggest challenge for anti-CTCs treatment is the interference of normal cells in whole blood, as it requires selective and efficient targeting of CTCs in the complex *in vivo* microenvironment. With the rapid development of biomembrane-coated nanotechnology, many biomembrane such as platelet membrane, neutrophil membrane

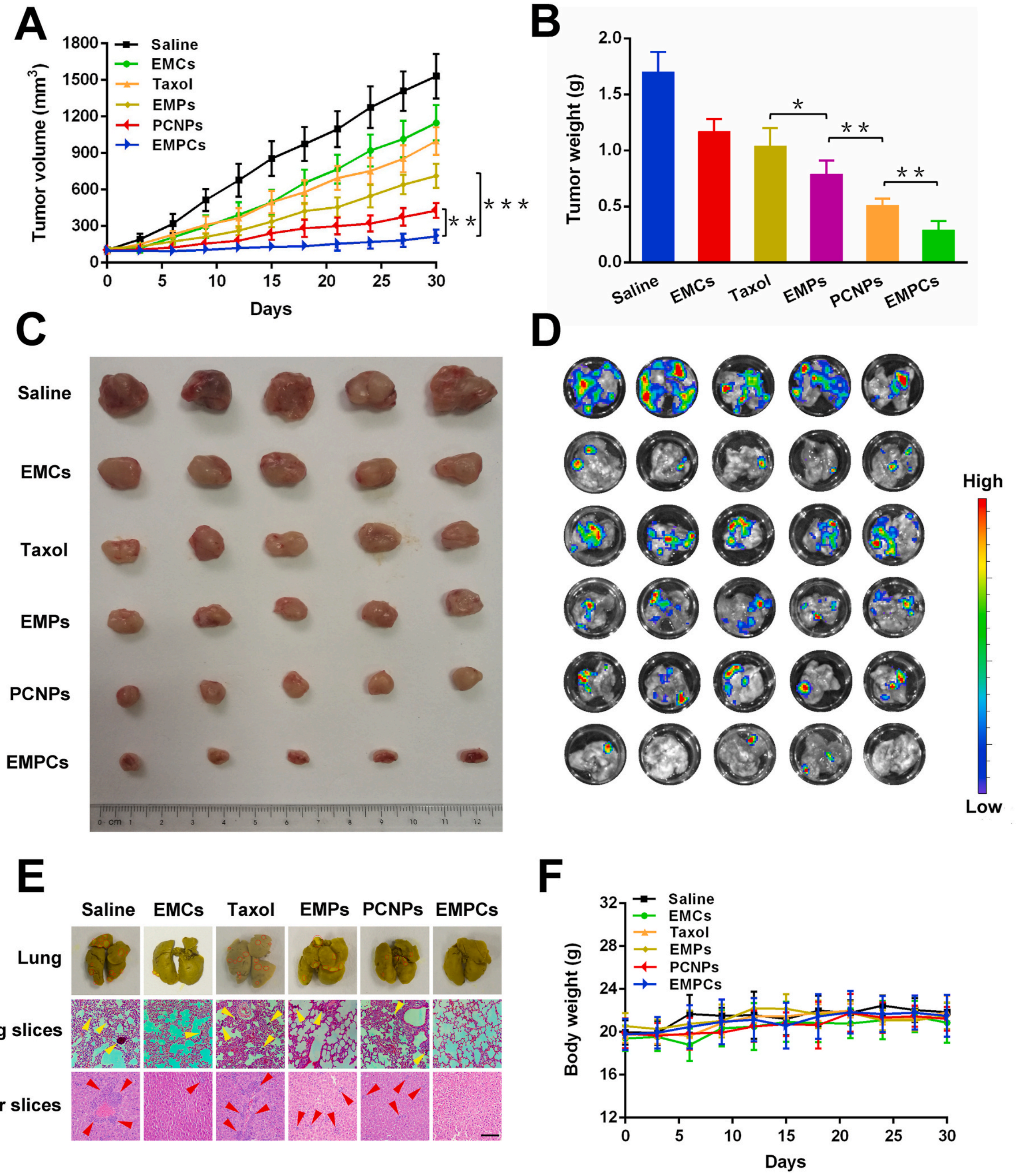

Fig. 8. (A) Growth curve of tumor volume for orthotopic MDA-MB-231 tumor model treated with various formulations. (B) The tumor weight change for orthotopic MDA-MB-231 tumor model during different treatments. (C) Graphs of tumors after the last treatment. (D) The *ex vivo* bioluminescent images of excised lungs after different treatments. (E) Photos of Bouin's staining for lungs and H&E staining for lung and liver slices at the end of treatment. Red circles demonstrate the visible metastatic site. Yellow and red arrows demonstrate the lung and liver metastases, respectively. Scale bar = 100 μm. (F) Changes in mice body weight (***$P < 0.001$, **$P < 0.01$, *$P < 0.05$, $n = 5$). (For interpretation of the references to colour in this figure legend, the reader is referred to the Web version of this article.)

was used to decorate drug-loaded nanoparticles and exhibited excellent CTCs capture capability due to the high-affinity membrane adhesion proteins. The EMPCs could track and capture the CTCs via adhesion molecule CD44. Following cellular uptake, the released CuB not only suppressed tumor metastasis via downregulation of the FAK/MMP signaling pathway but also remarkably enhanced intracellular ROS level to trigger the cascade amplified PTX chemotherapy, killing two birds with one stone.

As the time window in which CTCs invade the bloodstream can be very different and random, the anti-CTCs treatment must be applied timely after the diagnosis. Therefore, the efficient CTCs capture and early treatment are two key points for anti-CTCs treatment, and the proper anti-CTCs treatment could nip metastasis in the bud before the formation of metastatic foci. Due to the good CTCs-targeting capability, strengthened prodrug bioactivation, prolonged systemic circulation, enhanced tumor accumulation, and deeper tumor penetration, EMPCs exhibited improved primary tumor regression and excellent anti-metastasis activity in both orthotopic and xenograft MDA-MB-231 tumor models. Thus, the exosome-like prodrug nanoassembly, integrating metastasis inhibition and facilitated prodrug bioactivation into one platform, paves a new way for the mechanism-based inhibition of tumor metastasis.

Data availability

All relevant data are available from the authors.

Declaration of competing interest

The authors declare that they have no known competing financial interests or personal relationships that could have appeared to influence the work reported in this paper.

Acknowledgements

This work was supported by National Natural Science Foundation of China, No. 81773656 and U1608283, Liaoning Revitalization Talents Program, No XLYC1808017, Key projects of Technology Bureau in Shenyang, No 18400408, Key projects of Liaoning Province Department of Education, No. 2017LZD03.

Appendix A. Supplementary data

Supplementary data to this article can be found online at https://doi.org/10.1016/j.biomaterials.2020.120224.

Author contributions

K.W. and J.S. conceived the project. K.W., H.Y., X.Z., X.W., B.Y., Z.Z., J.Z. and Q.L. performed the experiments. K.W., H.Y. and C.L. analyzed the results. H.Z., Q.K., Y.W. and Z.H. provided useful suggestions to this work. K.W. and J.S. wrote the manuscript.

References

[1] R.L. Siegel, K.D. Miller, A. Jemal, Cancer statistics, CA Cancer J. Clin. 69 (1) (2019) 7–34.
[2] J. Shi, P.W. Kantoff, R. Wooster, O.C. Farokhzad, Cancer nanomedicine: progress, challenges and opportunities, Nat. Rev. Cancer 17 (1) (2017) 20–37.
[3] C. Liang, L. Xu, G. Song, Z. Liu, Emerging nanomedicine approaches fighting tumor metastasis: animal models, metastasis-targeted drug delivery, phototherapy, and immunotherapy, Chem. Soc. Rev. 45 (22) (2016) 6250–6269.
[4] M.W. Dewhirst, T.W. Secomb, Transport of drugs from blood vessels to tumour tissue, Nat. Rev. Cancer 17 (12) (2017) 738–750.
[5] Y. Gao, I. Bado, H. Wang, W. Zhang, J.M. Rosen, X.H. Zhang, Metastasis organotropism: redefining the congenial soil, Dev. Cell 49 (3) (2019) 375–391.
[6] P.S. Steeg, Targeting metastasis, Nat. Rev. Cancer 16 (4) (2016) 201–218.
[7] J. Massague, A.C. Obenauf, Metastatic colonization by circulating tumour cells, Nature 529 (7586) (2016) 298–306.
[8] S. Mathivanan, H. Ji, R.J. Simpson, Exosomes: extracellular organelles important in intercellular communication, J Proteom. 73 (10) (2010) 1907–1920.
[9] Z. Fan, K. Xiao, J. Lin, Y. Liao, X. Huang, Functionalized DNA enables programming exosomes/vesicles for tumor imaging and therapy, Small 15 (47) (2019), e1903761.
[10] E.A. Kwizera, R. O'Connor, V. Vinduska, M. Williams, E.R. Butch, S.E. Snyder, X. Chen, X. Huang, Molecular detection and analysis of exosomes using surface-enhanced Raman scattering gold nanorods and a miniaturized device, Theranostics 8 (10) (2018) 2722–2738.
[11] G. Cheng, W. Li, L. Ha, X. Han, S. Hao, Y. Wan, Z. Wang, F. Dong, X. Zou, Y. Mao, S. Y. Zheng, Self-assembly of extracellular vesicle-like metal-organic framework nanoparticles for protection and intracellular delivery of biofunctional proteins, J. Am. Chem. Soc. 140 (23) (2018) 7282–7291.
[12] J. Li, C. Sun, W. Tao, Z. Cao, H. Qian, X. Yang, J. Wang, Photoinduced PEG deshielding from ROS-sensitive linkage-bridged block copolymer-based nanocarriers for on-demand drug delivery, Biomaterials 170 (2018) 147–155.
[13] B. Sun, C. Luo, X. Zhang, M. Guo, M. Sun, H. Yu, Q. Chen, W. Yang, M. Wang, S. Zuo, P. Chen, Q. Kan, H. Zhang, Y. Wang, Z. He, J. Sun, Probing the impact of sulfur/selenium/carbon linkages on prodrug nanoassemblies for cancer therapy, Nat. Commun. 10 (1) (2019) 3211.
[14] S. Wang, Z. Wang, G. Yu, Z. Zhou, O. Jacobson, Y. Liu, Y. Ma, F. Zhang, Z.Y. Chen, X. Chen, Tumor-specific drug release and reactive oxygen species generation for cancer chemo/chemodynamic combination therapy, Adv. Sci. 6 (5) (2019) 1801986.
[15] C. Luo, B. Sun, C. Wang, X. Zhang, Y. Chen, Q. Chen, H. Yu, H. Zhao, M. Sun, Z. Li, H. Zhang, Q. Kan, Y. Wang, Z. He, J. Sun, Self-facilitated ROS-responsive nanoassembly of heterotypic dimer for synergistic chemo-photodynamic therapy, J. Control Release 302 (2019) 79–89.
[16] M. Ye, Y. Han, J. Tang, Y. Piao, X. Liu, Z. Zhou, J. Gao, J. Rao, Y. Shen, A tumor-specific cascade amplification drug release nanoparticle for overcoming multidrug resistance in cancers, Adv. Mater. 29 (38) (2017) 1702342.
[17] Q. Chen, G. Liu, S. Liu, H. Su, Y. Wang, J. Li, C. Luo, Remodeling the tumor microenvironment with emerging nanotherapeutics, Trends Pharmacol. Sci. 39 (1) (2018) 59–74.
[18] S. Sinha, S. Khan, S. Shukla, A.D. Lakra, S. Kumar, G. Das, R. Maurya, S.M. Meeran, Cucurbitacin B inhibits breast cancer metastasis and angiogenesis through VEGF-mediated suppression of FAK/MMP-9 signaling axis, Int. J. Biochem. Cell Biol. 77 (Pt A) (2016) 41–56.
[19] J. Liang, X.L. Zhang, J.W. Yuan, H.R. Zhang, D. Liu, J. Hao, W. Ji, X.Z. Wu, D. Chen, Cucurbitacin B inhibits the migration and invasion of breast cancer cells by altering the biomechanical properties of cells, Phytother Res. 33 (3) (2019) 618–630.
[20] W.-W. Luo, W.-W. Zhao, J.-J. Lu, Y.-T. Wang, X.-P. Chen, Cucurbitacin B suppresses metastasis mediated by reactive oxygen species (ROS) via focal adhesion kinase (FAK) in breast cancer MDA-MB-231 cells, Chin. J. Nat. Med. 16 (1) (2018) 10–19.
[21] G. Gu, H. Xia, Q. Hu, Z. Liu, M. Jiang, T. Kang, D. Miao, Y. Tu, Z. Pang, Q. Song, L. Yao, H. Chen, X. Gao, J. Chen, PEG-co-PCL nanoparticles modified with MMP-2/9 activatable low molecular weight protamine for enhanced targeted glioblastoma therapy, Biomaterials 34 (1) (2013) 196–208.
[22] H. Ye, K. Wang, M. Wang, R. Liu, H. Song, N. Li, Q. Lu, W. Zhang, Y. Du, W. Yang, L. Zhong, Y. Wang, B. Yu, H. Wang, Q. Kan, H. Zhang, Y. Wang, Z. He, J. Sun, Bioinspired nanoplatelets for chemo-photothermal therapy of breast cancer metastasis inhibition, Biomaterials 206 (2019) 1–12.
[23] N. Razavilar, P. Choi, Molecular dynamics study of the diffusivity of a hydrophobic drug Cucurbitacin B in pseudo-poly(ethylene oxide-b-caprolactone) micelle environments, Langmuir 30 (26) (2014) 7798–7803.
[24] H. Shao, H. Im, C.M. Castro, X. Breakefield, R. Weissleder, H. Lee, New technologies for analysis of extracellular vesicles, Chem. Rev. 118 (4) (2018) 1917–1950.
[25] G. Deng, Z. Sun, S. Li, X. Peng, W. Li, L. Zhou, Y. Ma, P. Gong, L. Cai, Cell-membrane immunotherapy based on natural killer cell membrane coated nanoparticles for the effective inhibition of primary and abscopal tumor growth, ACS Nano 12 (12) (2018) 12096–12108.
[26] H. Min, J. Wang, Y. Qi, Y. Zhang, X. Han, Y. Xu, J. Xu, Y. Li, L. Chen, K. Cheng, G. Liu, N. Yang, Y. Li, G. Nie, Biomimetic metal-organic framework nanoparticles for cooperative combination of antiangiogenesis and photodynamic therapy for enhanced efficacy, Adv. Mater. 31 (15) (2019), e1808200.
[27] H. Sun, J. Su, Q. Meng, Q. Yin, L. Chen, W. Gu, P. Zhang, Z. Zhang, H. Yu, S. Wang, Y. Li, Cancer-cell-biomimetic nanoparticles for targeted therapy of homotypic tumors, Adv. Mater. 28 (43) (2016) 9581–9588.
[28] C. Luo, J. Sun, D. Liu, B. Sun, L. Miao, S. Musetti, J. Li, X. Han, Y. Du, L. Li, L. Huang, Z. He, Self-assembled redox dual-responsive prodrug-nanosystem formed by single thioether-bridged paclitaxel-fatty acid conjugate for cancer chemotherapy, Nano Lett. 16 (9) (2016) 5401–5408.
[29] K. Wang, B. Yang, H. Ye, X. Zhang, H. Song, X. Wang, N. Li, L. Wei, Y. Wang, H. Zhang, Q. Kan, Z. He, D. Wang, J. Sun, Self-strengthened oxidation-responsive bioactivating prodrug nanosystem with sequential and synergistically facilitated drug release for treatment of breast cancer, ACS Appl. Mater. Interfaces 11 (21) (2019) 18914–18922.
[30] Y. Ji, J. Li, J. Zhao, S. Shan, C.C. Chu, A light-facilitated drug delivery system from a pseudo-protein/hyaluronic acid nanocomplex with improved anti-tumor effects, Nanoscale 11 (20) (2019) 9987–10003.
[31] Q. Hu, W. Sun, C. Qian, C. Wang, H.N. Bomba, Z. Gu, Anticancer platelet-mimicking nanovehicles, Adv. Mater. 27 (44) (2015) 7043–7050.
[32] G. Vona, A. Sabile, M. Louha, V. Sitruk, S. Romana, K. Schütze, F. Capron, D. Franco, M. Pazzagli, M. Vekemans, B. Lacour, C. Bréchot, P. Paterlini-Bréchot, Isolation by size of epithelial tumor cells, Am. J. Pathol. 156 (1) (2000) 57–63.
[33] X. Zhang, B. Sun, S. Zuo, Q. Chen, Y. Gao, H. Zhao, M. Sun, P. Chen, H. Yu, W. Zhang, K. Wang, R. Zhang, Q. Kan, H. Zhang, Z. He, C. Luo, J. Sun, Self-assembly of a pure photosensitizer as a versatile theragnostic nanoplatform for imaging-guided antitumor photothermal therapy, ACS Appl. Mater. Interfaces 10 (36) (2018) 30155–30162.
[34] T. Jiang, L. Chen, Y. Huang, J. Wang, M. Xu, S. Zhou, X. Gu, Y. Chen, K. Liang, Y. Pei, Q. Song, S. Liu, F. Ma, H. Lu, X. Gao, J. Chen, Metformin and docosahexaenoic acid hybrid micelles for premetastatic niche modulation and tumor metastasis suppression, Nano Lett. 19 (6) (2019) 3548–3562.
[35] M. Mendt, S. Kamerkar, H. Sugimoto, K.M. McAndrews, C.C. Wu, M. Gagea, S. Yang, E.V.R. Blanko, Q. Peng, X. Ma, J.R. Marszalek, A. Maitra, C. Yee, K. Rezvani, E. Shpall, V.S. LeBleu, R. Kalluri, Generation and testing of clinical-grade exosomes for pancreatic cancer, JCI Insight 3 (8) (2018).